Pharmaceutical Sciences and Drug Design
ISSN: 3062-4428
2025, Volume 5, Issue 2, Page No: 243-260

Available online at: www.galaxypub.co/page/journals

Galaxy Publication

Galaxy Publication

Synergistic Photodynamic–Chemotherapeutic Nanoplatform Induces Apoptosis to Counteract Drug-Resistant Breast Cancer

Ali Hassan[1]*, Noor Siddiqui[1], Bilal Khan[2], Sana Malik[1]

[1]Department of Drug Design and Pharmaceutical Innovation, Faculty of Pharmacy, Aga Khan University, Karachi, Pakistan.
[2]Department of Molecular Therapeutics and Drug Systems, Faculty of Pharmacy, Qatar University, Doha, Qatar.

***E-mail** ✉ ali.hassan@gmail.com

Received: 20 August 2026; **Revised:** 17 November 2026; **Accepted:** 19 November 2026

ABSTRACT

Standard chemotherapeutic regimens fail to provide adequate clinical outcomes in breast cancer owing to pervasive multidrug resistance. Here, we engineered dual-sensitization anti-resistant nanoparticles to manage recalcitrant breast cancer, seeking to capitalize on the combined benefits of photodynamic therapy and chemotherapy. A hyaluronic acid (HA) derivative and a chlorin e6 (Ce6) photosensitizer derivative were manufactured and validated by mass spectrometry. These compounds and the chemotherapeutic agent paclitaxel were co-formulated into nanoparticles using an emulsion-solvent evaporation procedure. The nanoparticles were evaluated with dynamic laser scattering, atomic force microscopy, and high-performance liquid chromatography (HPLC). Functional performance and mechanisms of action, both in vitro and in vivo, were assessed via flow cytometry, confocal/fluorescence microscopy, and a high-content screening platform. The designed dual-sensitization anti-resistant nanoparticles were spherical, measuring approximately 100 nm in diameter, and exhibited high paclitaxel encapsulation efficiency. They displayed potent suppression of drug-resistant breast cancer cell lines by boosting intracellular accumulation, generating synergistic anticancer activity between photodynamic therapy and chemotherapy, and triggering cell death through diverse signaling cascades. Acceptable in vivo efficacy, biocompatibility, and safety profiles were corroborated in murine tumor models. These dual-sensitization anti-resistant nanoparticles represent a viable strategy for addressing refractory breast cancer with precisely targeted treatment and limited systemic toxicity.

Keywords: Dual sensitization anti-resistant nanoparticles, Drug-resistant breast cancer, Apoptosis, Photodynamic therapy, Synergistic effect

How to Cite This Article: Hassan A, Siddiqui N, Bilal Khan B, Malik S. Synergistic Photodynamic–Chemotherapeutic Nanoplatform Induces Apoptosis to Counteract Drug-Resistant Breast Cancer. Pharm Sci Drug Des. 2025;5(2):243-60. https://doi.org/10.51847/Gz5VowOlkD

Introduction

Breast carcinoma constitutes the foremost hazard to female well-being, though currently available interventions do not yield satisfactory therapeutic results [1]. Clinical treatment failures are predominantly linked to metastatic dissemination and multidrug resistance [2-4]. As a cornerstone modality for malignant neoplasms, chemotherapy is critical for shrinking tumor mass and clearing postsurgical residual malignant cells. Nonetheless, unbound drug molecules in standard chemotherapy circulate indiscriminately throughout the organism, and recurrent administration of substantial doses fosters acquired drug resistance along with severe toxicities, ultimately dooming the therapeutic effort.

Broadly, multidrug resistance can be categorized into acquired and intrinsic forms. Acquired resistance emerges after repeated exposure to cytotoxic agents. It is chiefly defined by the heightened expression of ATP-binding cassette (ABC) transporters along the plasma membrane, namely p-glycoprotein (P-gp), multidrug resistance-associated proteins (MRPs), and breast cancer resistance protein (BCRP) [5]. The overabundance of these efflux pumps accelerates drug extrusion while curtailing cellular ingress, thereby eroding chemotherapeutic potency. By

contrast, intrinsic resistance pre-exists within malignant clones or stem-like cells before any drug challenge. It largely stems from elevated levels of anti-apoptotic Bcl-2 family proteins, such as Bcl-2 and Bcl-XL [6, 7]. These upregulated survival factors attenuate chemotherapy-inflicted injury and desensitize cancer cells. Hence, chemotherapy's impact is severely blunted.

Beyond chemotherapeutic approaches, photodynamic therapy has recently gained traction for treating superficial malignancies [8]. This modality employs light of a designated wavelength to excite a photosensitizer that has preferentially localized within the superficial tumor tissue [9]. Under oxygenated conditions within the tumor, the excited photosensitizer produces cytotoxic singlet oxygen through photodynamic reactions to annihilate neoplastic cells.

Chlorin e6 (Ce6) has attracted considerable attention as a photosensitizer of notable potential, one that can be produced starting from chlorophyll—a fact that underscores its expected biocompatibility. When illuminated by a suitable 660 nm laser, Ce6 becomes highly efficient at generating singlet oxygen, making it well suited for the development of photodynamic therapy platforms for tumor ablation [10, 11]. An additional advantage is the 660 nm laser's tissue-penetrating capability, which can penetrate several millimeters into human tissue [12]. Taken together, these characteristics make Ce6 a compelling candidate for breast cancer therapy, delivered either as monotherapy or in conjunction with other modalities.

The compound vitamin E polyethylene glycol succinate, abbreviated as TPGS, constitutes a water-dispersible derivative of vitamin E synthesized through esterification between the carboxyl moiety of vitamin E succinate and the terminal hydroxyl of polyethylene glycol. Within its molecular architecture, TPGS combines the lipophilic vitamin E domain with the hydrophilic polyethylene glycol extended chains. Its pronounced surfactant qualities and aqueous solubility contribute to a marked enhancement in gastrointestinal absorption of hydrophobic drugs, thereby boosting their bioavailability [13]. Investigations over the past few years have highlighted several unique functional properties of TPGS, notably its capacity to act as both an uptake promoter and a reversal agent for multidrug resistance [14].

Hyaluronic acid (HA) belongs to the class of acidic mucopolysaccharides and was originally isolated from the vitreous humor extracted from bovine eyes. Its unique molecular framework and physicochemical properties endow HA with a broad spectrum of physiological roles within the body, including lubrication of articular surfaces, regulation of vascular wall permeability, modulation of protein dynamics, and stimulation of wound repair processes [15, 16]. The high biocompatibility of HA makes it an attractive excipient in modern drug delivery technologies [17].

As a naturally derived anticancer compound, paclitaxel has been widely used for decades in the management of breast, ovarian, and lung malignancies. The mechanism through which paclitaxel operates involves interference with the normal dynamic equilibrium between tubulin and its dimeric forms in microtubules; it actively drives tubulin polymerization and fosters microtubule assembly while simultaneously preventing their disassembly. The net result is microtubule stabilization and consequent arrest of cancer cell mitosis. Despite its therapeutic value, paclitaxel's pronounced hydrophobicity and the emergence of resistant phenotypes have severely constrained its clinical applicability, underscoring the urgent need for new-generation paclitaxel formulations [18, 19].

Over the past several decades, nanoscale-based formulations have emerged as tools in the fight against cancer, including liposomes, polymersomes, and solid nanoparticles [20, 21]. These nano-engineered carriers can improve the bioavailability of agents with poor aqueous solubility, achieve prolonged residence in the circulatory compartment [22], and selectively localize at neoplastic sites. Consequently, such nano-formulations hold promise as an alternative line of attack against drug-resistant breast cancer.

In the investigation reported here, we set out to construct self-assembling nanoparticles that combine photodynamic therapy with chemotherapy to overcome drug resistance in breast cancer. To this end, an amphiphilic HA-α-TOS copolymer was prepared through covalent attachment of the hydrophobic molecule α-tocopherol succinate (α-TOS) onto the hydrophilic hyaluronic acid (HA) backbone. Separately, the photosensitizer Ce6 was chemically linked to TPGS1000, yielding a Ce6-TPGS1000 conjugate. Within the nanoparticle design, the α-TOS polymer constituted the hydrophobic core from which tumor microenvironment-responsive nanoparticles were fabricated, and both the Ce6-TPGS1000 conjugate and the chemotherapeutic payload paclitaxel were co-incorporated. The convergence of photodynamic therapy and chemotherapy was anticipated to bring their combined therapeutic power to bear on drug-resistant breast cancer cells.

Materials and Methods

Materials and cell lines

Paclitaxel and Ce6 were obtained from Macklin Biochemical Co., Ltd. (Shanghai, China). TPGS1000 was supplied by Energy Chemical Co., Ltd. (Shanghai, China). HA (molecular weight 4000 Da) and α-TOS were procured from Yuanye Bio-Technology Co., Ltd (Shanghai, China). Roswell Park Memorial Institute 1640 (RPMI-1640) culture medium, phosphate-buffered saline (PBS), trypsin–EDTA solution, penicillin/streptomycin preparation, and fetal bovine serum (FBS) were all sourced from Zhong Sheng Ao Bang Co., Ltd. (Beijing, China). All remaining reagents were obtained from commercial sources and used directly without further purification.

The human breast carcinoma line MCF-7 was acquired from the Institute of Basic Medical Sciences, Chinese Academy of Medical Sciences (Beijing, China). The drug-resistant variant MCF-7/adr was obtained from the Institute of Hematology & Blood Diseases Hospital, Chinese Academy of Medical Sciences (Tianjin, China). Both MCF-7 and MCF-7/adr cells were propagated in RPMI-1640 medium supplemented with 10% FBS and maintained in a humidified incubator at 37°C under 5% CO_2. Throughout the experimental procedures, MCF-7 and MCF-7/adr cultures were maintained in the exponential growth phase, and periodic mycoplasma tests were conducted to ensure cultures remained free of contamination.

Synthesis of HA-α-TOS and Ce6-TPGS1000 conjugates

To begin the synthetic sequence, 0.2 mmol of α-TOS was taken up in 1 mL of N,N-dimethylformamide (DMF), after which 0.3 mmol each of 1-(3-dimethylaminopropyl)-3-ethylcarbodiimide hydrochloride (EDC) and n-hydroxysuccinimide (NHS) were introduced in succession. The entire setup was maintained under a nitrogen blanket and left to proceed at ambient temperature for 12 h. In parallel, a separate vessel was charged with 2 mmol of ethylenediamine (EDA) dissolved in ice-cold DMF, and this solution was transferred dropwise into the activated α-TOS mixture. Stirring continued for a further 12 h under nitrogen at room temperature. Upon completion, the reaction mixture was placed in a dialysis membrane and dialyzed for 48 h to remove unreacted starting materials, after which the retained fraction was freeze-dried to isolate TOS-NH_2. The next stage involved dissolving 0.3 mmol of HA in formamide heated to 45°C in a water bath. To this HA solution, 0.6 mmol of EDC and 0.6 mmol of NHS were added to promote carboxyl activation over 6 hours. TOS-NH_2 (0.6 mmol), dissolved beforehand in 8 mL of DMF, was then added dropwise at a 1:2 molar ratio, and the reaction was allowed to proceed under gentle agitation with nitrogen purging at room temperature for 24 h. The resulting mixture was poured into excess chilled acetone to induce precipitation; the precipitate was rinsed with additional cold acetone, reconstituted in water, and dialyzed against water for 48 h through a dialysis membrane. The retained material was collected and lyophilized, affording the final product, HA-α-TOS.

For the preparation of the photosensitizer conjugate, Ce6 (0.33 mmol), TPGS1000 (0.66 mmol), dicyclohexylcarbodiimide (DCC, 0.40 mmol), and 4-dimethylaminopyridine (DMAP, 0.006 mmol) were dissolved in 3 mL of dimethyl sulfoxide (DMSO). This combined solution was stirred for 18 h at room temperature under a nitrogen atmosphere, yielding the crude Ce6-TPGS1000 material. Solids were removed from the crude mixture by filtration, and the clarified filtrate was loaded into a dialysis tube. A two-stage dialysis was conducted—first against DMSO for a full day, then against deionized water for an equivalent duration. The contents retained inside the tube at the end of this process were lyophilized, yielding the purified Ce6-TPGS1000. Both final products were authenticated by laser desorption ionization time-of-flight mass spectrometry (MALDI-TOF-MS; ABI 4800 Plus, Applied Biosystems, CA, USA).

Fabrication and physicochemical characterization of nanoparticles

The dual-sensitization anti-resistant nanoparticles were assembled employing an emulsion-solvent evaporation technique. Ten milligrams of HA-α-TOS, together with 5 mg of Ce6-TPGS1000, were weighed, dissolved in 5 mL of distilled water, and agitated in a vortex mixer for 1 min to achieve thorough dissolution. One milligram of paclitaxel was separately solubilized in 200 μL of chloroform. An oil-in-water (O/W) emulsion was then formed by subjecting the combined phases to ultrasonication for 5 min while kept chilled on an ice bath. The prepared O/W emulsion was evaporated overnight under slow magnetic stirring at room temperature, after which the crude dual-sensitization anti-resistant nanoparticles were harvested. Nanoparticles loaded solely with paclitaxel or solely with Ce6 were manufactured following identical steps, with the omission of the Ce6-TPGS1000 component or the paclitaxel component, respectively, from the formulation.

The morphological characteristics of the nanoparticles were visualized under an atomic force microscope (AFM, SPI3800N series SPA-400, Tokyo, Japan). Particle dimensions, size distribution, and zeta potential were assessed using a Nano ZS90 Zetasizer (Malvern Instruments Ltd, Malvern, UK).

Separation of the nanoparticle-encapsulated drug fractions from free paclitaxel or free Ce6-TPGS1000 was accomplished by dextran gel chromatography. Quantification of paclitaxel and Ce6-TPGS1000 in the separated fractions was performed using HPLC instrumentation equipped with a UV detector (LC-20AT, Shimadzu, Kyoto, Japan). The encapsulation efficiency (EE%) was derived from the following expression: EE% = (Wencapsulated/Wtotal) × 100%, where Wencapsulated signifies the mass of drug housed within the nanoparticle population, and Wtotal denotes the starting mass of drug used in the formulation.

To probe nanoparticle stability over time, nanoparticles were dispersed in both normal saline and 50% FBS solution. Aliquots were drawn from each medium at scheduled intervals of 0, 6, 12, 24, and 48 h, and the particle size at each time point was recorded on the Nano ZS90 Zetasizer (Malvern Instruments Ltd, Malvern, UK).

The profile of paclitaxel release from the nanoparticles under in vitro conditions was monitored using a dialysis-based method against PBS (pH = 7.4) containing 10% FBS. Paclitaxel that had diffused out was measured at designated intervals by HPLC (LC-20AT, Shimadzu, Kyoto, Japan).

Cytotoxicity testing

Dark cytotoxicity was evaluated by seeding MCF-7 and MCF-7/adr cells at 5×10^3 cells per well in 96-well plates, then maintaining them in complete RPMI-1640 medium for 24 hours to allow attachment and growth. Four test formulations—free paclitaxel, paclitaxel nanoparticles, Ce6 nanoparticles, and dual sensitization anti-resistant nanoparticles—were then introduced to the cells at escalating dose levels spanning 0 to 50 μg/mL (standardized to paclitaxel equivalent mass), with exposure lasting 48 hours in the absence of light.

Photodynamic cytotoxicity was measured by first plating MCF-7 and MCF-7/adr cells in 96-well plates using the same seeding procedure. The plated cells were subsequently challenged with the four formulation types at varying strengths (0–50 μg/mL, expressed as paclitaxel equivalents) for 12 hours. Once the treatment medium had been replaced with fresh culture fluid, a 660 nm laser beam (50 mW) was directed onto each well for 10 minutes, and the plates were returned to incubation conditions for a further 36 hours.

At the conclusion of each incubation period, spent media were aspirated from the wells. A volume of 100 μL of ice-chilled 10% trichloroacetic acid (TCA) was dispensed into each well, and cell fixation was performed at 4°C for a minimum of 1 hour. Residual TCA was subsequently eliminated by rinsing all wells five times with deionized water. The plates were left to dry completely before 100 μL of 0.4% sulforhodamine B (SRB, formulated in 1% acetic acid) was added to stain the adherent fixed cells, with staining allowed to proceed at room temperature over 20 minutes. Unincorporated SRB dye was washed away using five rinses of 1% acetic acid per well. After the plates had dried thoroughly, the protein-bound SRB was released by introducing 200 μL of 10 mmol/L Tris Base (pH = 10.5) to each well. Absorbance values for individual wells were recorded at 540 nm on a microplate reader. The percentage of surviving cells was employed as the metric of treatment toxicity toward the breast cancer lines and was computed as shown below:

$$\text{Survival rate (\%)} = [\text{absorbance of treated wells (A540 nm)} / \text{absorbance of untreated control wells (A540 nm)}] \times 100 \quad (1)$$

Live/dead visualization of synergistic activity

To directly image photodynamic cell killing, a live/dead dual-fluorescence assay was carried out post-irradiation. MCF-7/adr cells were initially plated at 1.5×10^5 cells per well in 12-well plates and incubated in complete RPMI-1640 medium for 24 hours. Free paclitaxel, paclitaxel nanoparticles, Ce6 nanoparticles, and dual sensitization anti-resistant nanoparticles were each applied at a fixed strength of 50 μg/mL (relative to paclitaxel equivalent concentration) for a 12-hour treatment window. Culture media were refreshed before the designated wells were illuminated with a 660 nm laser (100 mW) for 10 minutes.

The cells were then incubated for an additional 12 hours, after which they were co-stained with calcein AM and ethidium homodimer-1. A 30-minute staining interval was allowed before the specimens were examined using a fluorescence microscope (DMi8, Leica, Wetzlar, Germany).

Nanoparticle internalization by MCF-7/Adr cells

Cellular entry of nanoparticles into the drug-resistant MCF-7/adr line was monitored by confocal laser scanning microscopy and flow cytometry, using coumarin as a fluorescent tracer. For these uptake studies, nanoparticles were prepared according to the standard protocol, except that coumarin was used instead of paclitaxel as the encapsulated payload. MCF-7/adr cells in the logarithmic growth phase were transferred into confocal dishes at a concentration of 1.5×10^5 cells per well and cultured for 24 hours. The four treatment groups—normal saline, coumarin nanoparticles, Ce6 nanoparticles, and dual sensitization anti-resistant nanoparticles—were each administered at a uniform dose of 2 μg/mL (normalized to coumarin equivalence). At the 6-hour mark, treatment solutions were withdrawn, and the dishes were gently washed three times with PBS. Nuclei were counterstained by applying Hoechst 33342 (2 μg/mL) for 10 minutes. The intracellular fluorescence signal from coumarin, along with its spatial localization, was captured using a confocal microscope (FV-10i-O, Olympus, Tokyo, Japan).

To quantify uptake kinetics via flow cytometry, MCF-7/adr cells were dispensed into 6-well culture plates at 4×10^5 cells per well. Following a 24-hour establishment period, the wells received normal saline, coumarin nanoparticles, Ce6 nanoparticles, or dual sensitization anti-resistant nanoparticles, all at a coumarin-equivalent level of 2 μg/mL. Cells were detached and harvested from the plates at serial time intervals of 1, 2, 4, and 8 hours post-addition, then immediately analyzed on a FACS Calibur™ flow cytometer (BD Biosciences, CA, USA).

Apoptosis evaluation in cultured cells

For flow cytometric assessment of apoptosis, drug-resistant MCF-7/adr cells were plated at 4×10^5 cells per well in 6-well plates and incubated for 24 hours to allow adherence. A panel of four test articles—free paclitaxel, paclitaxel nanoparticles, Ce6 nanoparticles, and dual-sensitization anti-resistant nanoparticles—was applied at a uniform concentration of 50 μg/mL (calibrated to paclitaxel equivalence) and allowed to act on the cells for 12 hours. Following this exposure window, the treatment-containing medium was discarded and replaced, and the cell monolayers were subjected to a 10-minute irradiation cycle using a 660 nm laser at 50 mW. A subsequent 24-hour recovery incubation was performed before the cells were harvested and co-labeled with propidium iodide (PI) and Annexin V-Alexa Fluor 488 (Invitrogen, CA, USA) according to the protocol supplied with the kit. Stained specimens were immediately analyzed on a flow cytometer, with data acquisition completed within 1 hour (Gallios, Beckman Coulter, CA, USA).

In a complementary experiment designed for imaging-based apoptosis detection, MCF-7/adr cells were placed into 12-well plates at 2×10^5 cells per well and allowed to grow for 24 hours. Five experimental conditions were established: PBS vehicle control, free paclitaxel, paclitaxel nanoparticles, Ce6 nanoparticles, and dual-sensitization anti-resistant nanoparticles, each delivered at 50 μg/mL, normalized to paclitaxel content. After 12 hours of exposure, the media were exchanged for fresh culture fluid, and the plates were illuminated with a 660 nm laser (50 mW, 10 min). A further 6-hour incubation period elapsed before the cells were simultaneously stained with Hoechst 33342 and Mitotracker Red (Invitrogen, CA, USA) and visualized on the Operetta high-content screening platform (PerkinElmer, MA, USA).

Profiling of apoptosis-related protein expression

MCF-7/adr cells were seeded into 96-well microplates and allowed to propagate until reaching approximately 40–50% confluency. Five treatment arms were then applied: normal saline, free paclitaxel, paclitaxel nanoparticles, Ce6 nanoparticles, and dual-sensitization anti-resistant nanoparticles, each at a paclitaxel-equivalent concentration of 50 μg/mL. The 12-hour treatment phase was concluded by aspirating and refreshing the medium, after which plates designated for photodynamic activation were exposed to a 660 nm laser (50 mW, 10 min). Cells were incubated for an additional 12 hours before immunofluorescence processing. The processing sequence comprised fixation in 4% paraformaldehyde, permeabilization with Triton X-100, and blocking with goat serum. An overnight incubation was performed with a set of primary antibodies against caspase 3, caspase 8, caspase 9, Mcl-1, Bax, and cytochrome c (Sangon, Shanghai, China). Detection relied on an Alexa Fluor 488-conjugated secondary antibody (Invitrogen, CA, USA), with nuclei counterstained with DAPI (KeyGene BioTech, Nanjing, China). Quantitative readout of Alexa Fluor 488 fluorescence intensity per well was obtained using the Operetta high-content screening system (PerkinElmer, MA, USA).

In vivo therapeutic performance of nanoparticles

Female Nu/Nu nude mice were procured from Beijing Vital River Laboratory Animal Technology Co., Ltd. (Beijing, China). The entire animal experimentation was conducted in accordance with ethical principles and with

the explicit approval of the Bioethics Committee of the Beijing Institute of Petrochemical Technology. To generate tumor models, 1×10^7 MCF-7/adr cells were implanted subcutaneously into the right flank of each Nu/Nu female nude mouse at 6 weeks of age. Serial tumor dimensions were obtained using digital calipers and converted to volume estimates using the equation length × width²/2. When tumors attained a size of approximately 500 mm³, they were surgically harvested, minced, and serially passaged into naïve recipient nude mice. Upon reaching a volume of roughly 100 mm³ in the passage animals, the mice were stratified by randomization into five cohorts, each containing six individuals. Intravenous dosing was performed via the tail vein, delivering normal saline, free paclitaxel, paclitaxel nanoparticles, Ce6 nanoparticles, or dual-sensitization anti-resistant nanoparticles, all formulated to achieve a paclitaxel-equivalent dosage of 5 mg/kg. The treatment regimen consisted of five administrations spaced one day apart, on an every-other-day schedule. Twenty-four hours after each injection, mice in the Ce6 nanoparticle and dual-sensitization anti-resistant nanoparticle arms were subjected to a 5-minute session of 660 nm laser irradiation (100 mW), with the beam spot positioned precisely over the palpable tumor mass. Both tumor volumes and mouse body weights were documented daily throughout the study. Tumor growth kinetics were expressed as a relative tumor volume ratio according to the formula: relative ratio to tumor volume (%) = Vn/V14 × 100, where Vn corresponds to the tumor volume measured on day n, and V14 represents the baseline tumor volume recorded on day 14 at the commencement of dosing.

Statistical methodology

One-way analysis of variance (ANOVA) was applied to evaluate overall differences across treatment groups. Where significant main effects were identified, post hoc pairwise comparisons were conducted using the Bonferroni correction for multiple comparisons. All data are presented in the form of mean ± standard deviation (SD).

Results and Discussion

Verification of HA-α-TOS and Ce6-TPGS1000 structures

Figure 1 presents the synthetic strategies and confirmatory analyses for the two synthesized materials, HA-α-TOS and Ce6-TPGS1000. The MALDI-TOF-MS spectral data obtained for both HA-α-TOS and Ce6-TPGS1000 offered robust validation that the constituent modules had been covalently joined as intended.

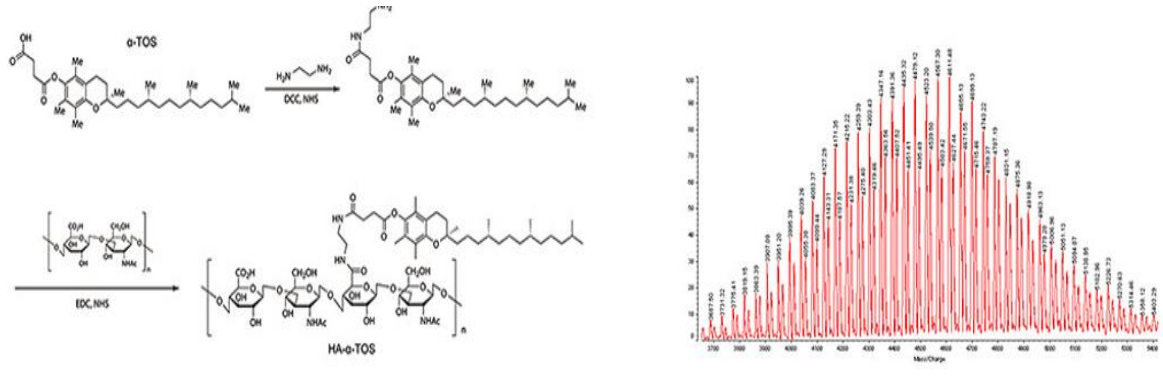

a) b)

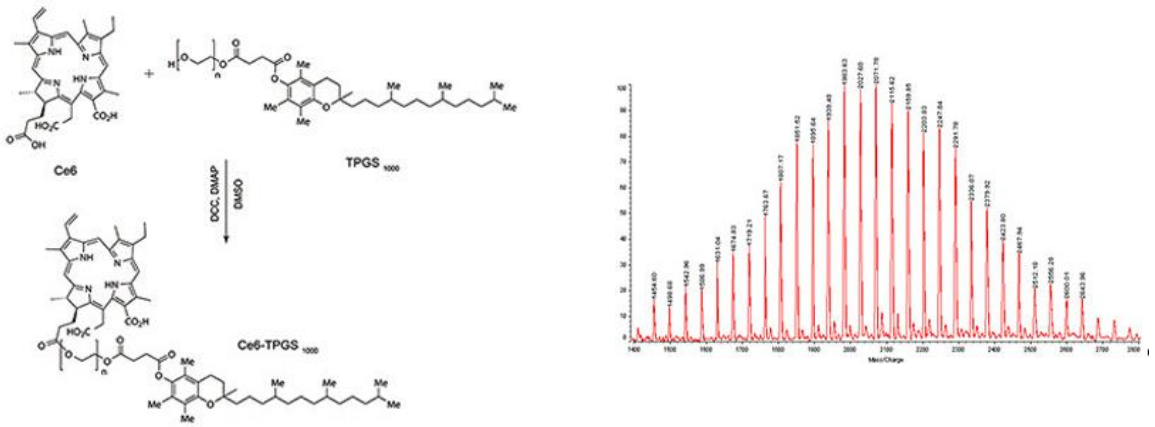

c) d)

Figure 1. Depicts the synthesis and characterization of HA-α-TOS (Panels a and b) and Ce6-TPGS1000 (Panels c and d).

Nanoparticle characterization

Figure 2 compiles the physicochemical characterization data for the various nanoparticle formulations. A schematic representation of the structural organization within the dual-sensitization anti-resistant nanoparticles is shown in **Figure 2a**. AFM visualization **(Figure 2b)** revealed that all three nanoparticle types adopted a spherical morphology, with diameters of approximately 80 nm for paclitaxel-only nanoparticles and approximately 100 nm for both Ce6 nanoparticles and the dual-sensitization anti-resistant nanoparticles. Size distribution profiles and surface charge measurements acquired via dynamic laser scattering (DLS) are shown in **Figures 2c and 2d**, with the corresponding numerical summaries tabulated in **Table 1**. Mean hydrodynamic diameters of 68.1 ± 3.2 nm, 92.4 ± 4.3 nm, and 108.5 ± 5.5 nm were recorded for paclitaxel nanoparticles, Ce6 nanoparticles, and dual sensitization anti-resistant nanoparticles, respectively. Across the three systems, zeta potential values were confined to a narrow band extending from −15.9 ± 0.4 mV down to −14.3 ± 0.5 mV. Such modestly electronegative surface charges would likely help maintain colloidal dispersions against aggregation over extended periods. The polydispersity index (PDI) remained below 0.25 for each preparation, indicating a narrow distribution and favorable uniformity of the particle populations. In all nanoparticle variants, the fraction of paclitaxel successfully entrapped exceeded 95%, whereas the Ce6-TPGS1000 loading efficiency was close to 80%. **Figure 2e** documents how mean particle dimensions shifted over time when the nanoparticles were placed in different suspending media. Negligible size drift was observed for Ce6 nanoparticles and dual-sensitization anti-resistant nanoparticles, in contrast to the progressive size increase observed for the paclitaxel nanoparticle formulation. The kinetics of paclitaxel egress from the nanoparticles under in vitro sink conditions in PBS (pH = 7.4) are traced in **Figure 2f**. At the 48-hour sampling point, the cumulative fraction of paclitaxel released was 6.0 ± 0.5% for paclitaxel nanoparticles and 0.5 ± 0.1% for the dual-sensitization anti-resistant nanoparticles. The limited extent of drug release measured at 48 hours suggests that the particulate carriers retain their structural integrity en route to the designated target tissue.

Table 1. Characterization of prepared nanoparticles

Nanoparticle formulation	Ce6-TPGS1000 encapsulation efficiency (%)	Paclitaxel encapsulation efficiency (%)	Surface charge (mV)	Polydispersity index	Hydrodynamic diameter (nm)
Paclitaxel nanoparticles	—	98.5 ± 0.3	−15.9 ± 0.4	0.184 ± 0.012	68.1 ± 3.2
Ce6 nanoparticles	82.1 ± 0.4	—	−15.2 ± 0.6	0.225 ± 0.023	92.4 ± 4.3
Dual-sensitization anti-resistance nanoparticles	78.5 ± 1.2	97.6 ± 0.5	−14.3 ± 0.5	0.237 ± 0.019	108.5 ± 5.5

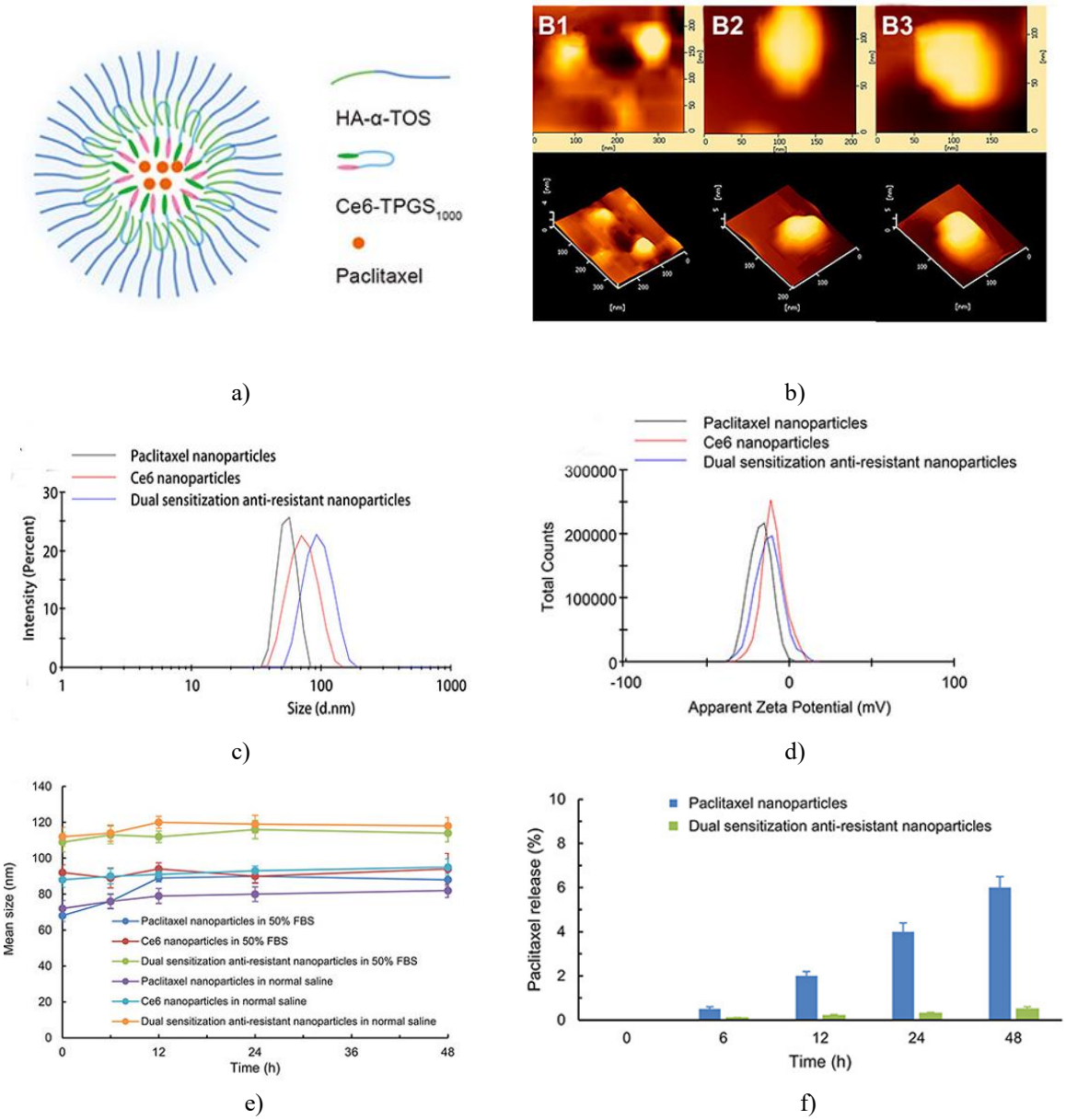

Figure 2. Characterization of prepared nanoparticles: (a) Schematic diagram of dual sensitization anti-resistance nanoparticles; (b) AFM images of paclitaxel nanoparticles (B1), Ce6 nanoparticle (B2), and dual sensitization anti-resistance nanoparticle (B3); (c) the size distribution of prepared nanoparticles; (d) the zeta potentials of prepared nanoparticles; (e) mean particle size of prepared nanoparticles in normal saline and 50% FBS solution; (f) in vitro release of paclitaxel in PBS (pH = 7.4). All the data are presented as the mean ± standard deviation (n = 3).

Growth inhibition of breast cancer cell lines

Figure 3 displays the toxicity profiles elicited by the different treatments against MCF-7 cells **(Figures 3a and 3b)** and the drug-insensitive MCF-7/adr derivative line **(Figures 3c and 3d).** Parallel experiments were run either with complete light exclusion **(Figures 3a and 3c)** or with a 10-minute step of 660 nm laser illumination **(Figures 3b and 3d)**. Under dark incubation, MCF-7 cells exhibited marked sensitivity toward the chemotherapeutic paclitaxel, yet remained entirely unaffected by the Ce6 constituent on its own **(Figure 3a).** All paclitaxel-inclusive formulations suppressed cell growth in a concentration-dependent manner, with the unformulated free drug yielding the most pronounced antiproliferative effect. The nearly complete absence of dark toxicity from Ce6 nanoparticles underscored the acceptable biocompatibility inherent to the synthesized components.

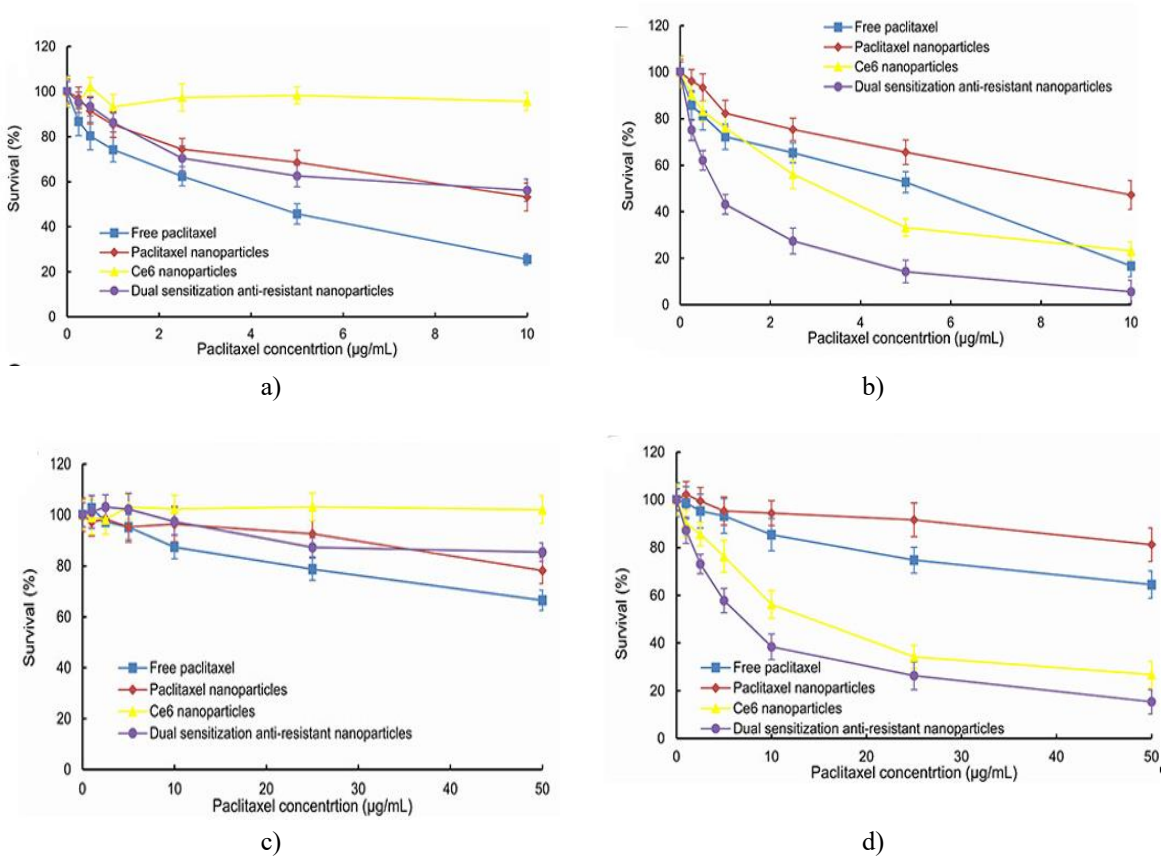

Figure 3. In vitro cytotoxic effect after treating with varying formulations. Dual-sensitization nanoparticles and other formulations were applied to human breast cancer MCF-7 cells (a and b) or drug-resistant human breast cancer MCF-7/adr cells (c and d) for 48 h. The cells were treated in the dark (a and c) or irradiated with a 660nm laser (b and d) for 10 min. Data are presented as the mean ± standard deviation (n = 6).

The antiproliferative responses measured across the different treatment groups upon 660 nm laser activation are documented in **Figure 3b.** Whether light was applied or not made almost no difference to the cytotoxic activity of either free paclitaxel or the paclitaxel nanoparticle formulation—a logical observation given that paclitaxel does not respond to photoexcitation. The situation was entirely different, however, for preparations containing Ce6: both Ce6-only nanoparticles and the dual sensitization anti-resistant nanoparticles exhibited dramatically elevated cell-killing capabilities once the laser was turned on. Of particular importance, the dual sensitization of anti-resistant nanoparticles gave rise to a powerful cooperative interaction between the two therapeutic principles, with chemotherapy and photodynamic therapy mutually amplifying each other's effects.

Turning to the drug-resistant MCF-7/adr variant, **Figure 3c** presents the cytotoxicity data collected under dark conditions. These cells proved to be fundamentally different from the parental MCF-7 line, showing broad cross-resistance that rendered them essentially unresponsive to all anticancer insults. Regardless of the formulation tested, the level of growth suppression achieved against MCF-7/adr cells remained disappointingly low—a shortcoming that persisted even at the highest paclitaxel dose used in the study (50 μg/mL).

The results obtained when these same resistant cells were challenged with 660 nm photoactivation are shown in **Figure 3d**. Predictably, both the free drug and the paclitaxel nanoparticle preparation continued to show little tumor cell killing, a direct consequence of the well-established multidrug resistance inherent to the MCF-7/adr phenotype. What stood out, however, was the remarkable augmentation of anticancer potential observed in the groups that incorporated the photosensitizer: both Ce6 nanoparticles and the dual-sensitization anti-resistant nanoparticles became substantially more effective after light exposure. Ranking the treatment arms by antiproliferative strength placed the dual sensitization anti-resistant nanoparticles at the very top, underscoring the significant synergy that emerged from the combined treatment approach.

Live/dead staining confirms cooperative cell destruction

The effects of the various nanoparticle treatments on MCF-7/adr cell survival were further evaluated by live/dead fluorescence imaging, with results separated into dark-incubated **(Figure 4a)** and laser-irradiated **(Figure 4b)** samples. When light was excluded throughout the experiment, the resistant cells flourished regardless of the nanoparticle type to which they had been exposed, and dying cells were rare across the board. This picture was consistent with the dark cytotoxicity measurements, which likewise indicated negligible toxicity for all formulations against this cell line. Once a 660 nm laser was introduced into the protocol, the landscape of cell viability shifted radically **(Figure 4b).** Wells treated with paclitaxel nanoparticles continued to show predominantly intact, living cells—hardly surprising given both paclitaxel's laser insensitivity and the drug-resistant phenotype. In sharp contrast, the regions hit by the laser in wells that had received Ce6 nanoparticles or dual-sensitization anti-resistant nanoparticles showed extensive cell death. A small number of viable cells did, however, remain scattered within the laser-exposed territory **(Figure 4b)** (identifiable as green-fluorescent spots surrounded by expanses of red fluorescence emanating from dead neighbors). The group that consistently showed the sparsest residual live cell population after irradiation was the one treated with the dual sensitization anti-resistant nanoparticles, reaffirming their superior therapeutic effectiveness.

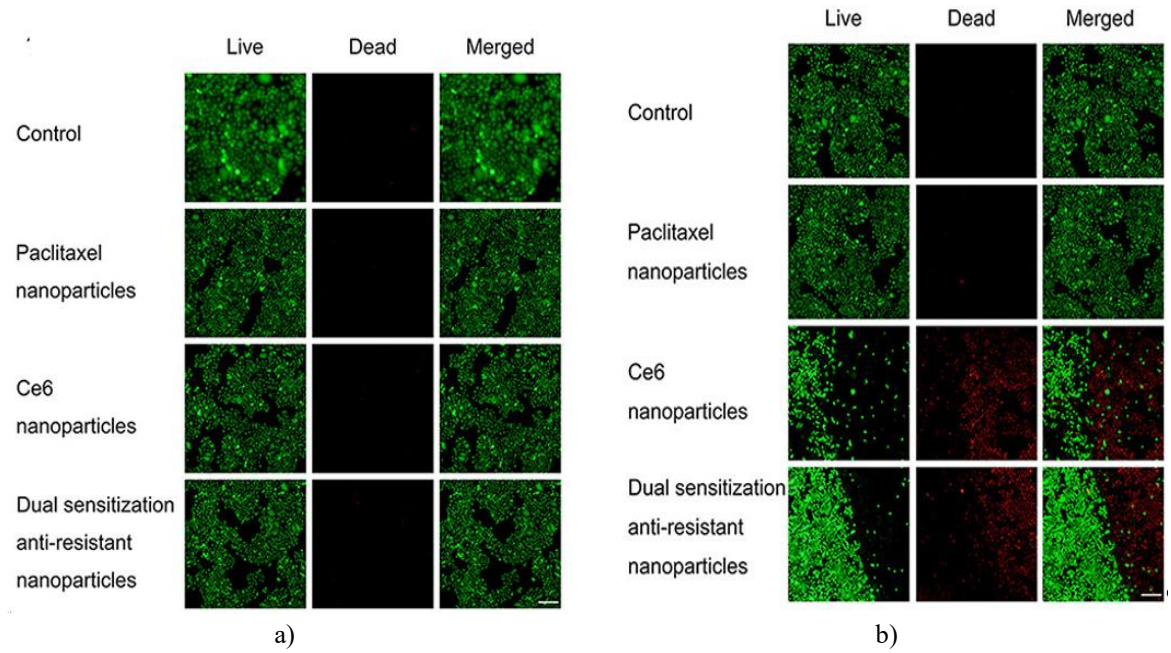

Figure 4. Survival status of drug-resistant MCF-7/adr cells after treatment with varying nanoparticles in dark conditions (a) and after laser irradiation (b). Notes: The cells were observed by a fluorescence microscope. The green fluorescence indicates live cells stained by calcein AM, while the red fluorescence was emitted by the dead cells stained by ethidium homodimer. The dashed lines indicate the laser boundary. Scale bar = 200 μm.

Quantitative and qualitative analysis of nanoparticle internalization

The extent to which the resistant breast cancer line took up coumarin-tagged nanoparticles was assessed, and the results are summarized in **Figure 5**. Confocal imaging of MCF-7/adr cells following exposure to the different coumarin-containing preparations revealed striking differences in both the intensity and the subcellular pattern of green fluorescence **(Figure 5a).** When coumarin was presented to cells in its free, unformulated state, the resulting intracellular fluorescent signal proved exceedingly dim, suggesting that only minimal amounts of the dye molecule could traverse the plasma membrane under these conditions. By polar contrast, robust and widespread green emission filled the cytoplasm when coumarin was delivered via either coumarin nanoparticles or dual coumarin nanoparticles—a clear indication that nanoparticle encapsulation dramatically enhanced cellular entry. Moreover, careful inspection of the fluorescence micrographs revealed distinct punctate green structures within the cytoplasm in both nanoparticle-treated groups, a pattern highly consistent with endocytosis rather than simple passive permeation.

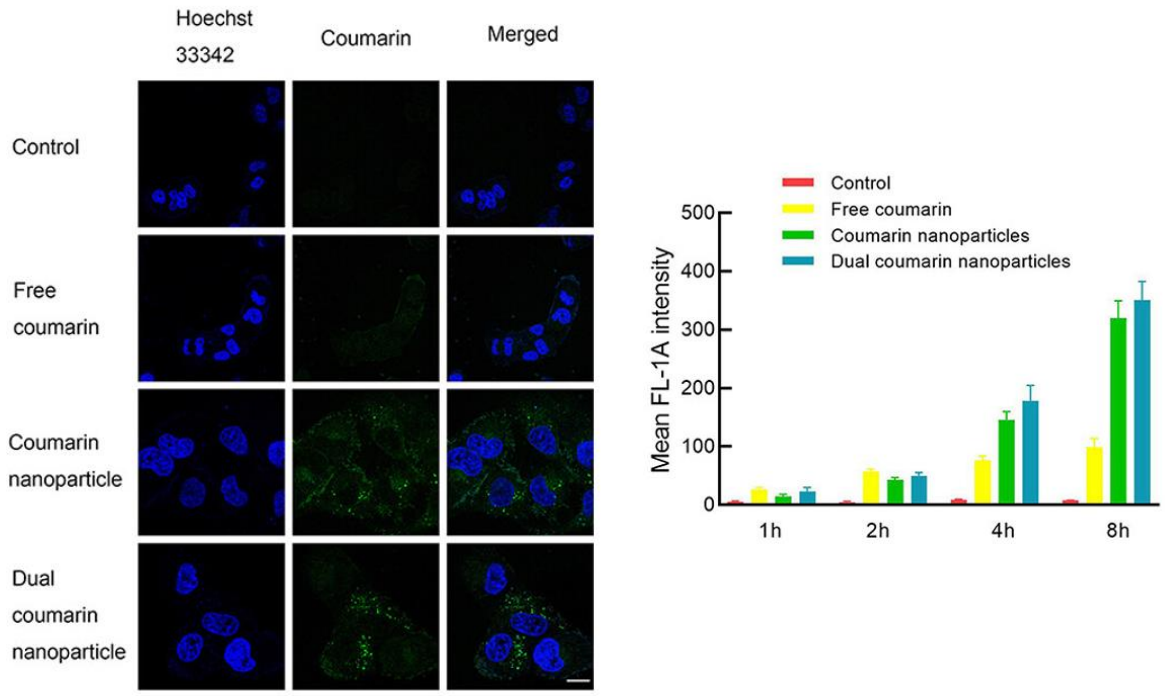

a) b)

Figure 5. Cellular uptake of various coumarin nanoparticles: (a) Confocal images of various coumarin nanoparticles in the drug-resistant MCF-7/adr cells after treatment with coumarin nanoparticles. Scale bar = 25 μm; (b) mean fluorescence intensity of drug-resistant MCF-7/adr cells after exposure to varying coumarin nanoparticles for 1–8 h.

Figure 5b, together with the accompanying **Table 2,** charts the time course of mean fluorescence intensity within MCF-7/adr cells over a monitoring period spanning 1 to 8 hours following the introduction of each coumarin preparation. A clear-cut temporal dependence governing cellular coumarin accumulation was documented in all cases, with increasingly longer exposures yielding correspondingly higher intracellular levels. Where free coumarin was concerned, however, the uptake trajectory flattened out upon reaching the 8-hour sampling point, a behavior characteristic of a saturable transport process operating at its maximal capacity. The temporal profiles observed for coumarin nanoparticles and dual coumarin nanoparticles told a different story entirely: rather than leveling off, the fluorescent readout continued to climb throughout the entire observation window, with no indication of approaching a ceiling. Such a pattern implies that these nanocarriers exploit a fundamentally different—and non-saturable—mechanism for cellular entry. This mechanistic distinction very likely lies at the heart of the markedly enhanced intracellular delivery performance achieved by the nanoparticle-based platforms.

Table 2 Mean fluorescence intensity of MCF-7/Adr cells after various nanoparticles' exposure

Time (h)/Groups	Dual coumarin nanoparticles	Coumarin nanoparticles	Free coumarin	Control
1	23.2 ± 6.7	14.7 ± 3.5	26.4 ± 3.2	5.6 ± 1.2
2	49.8 ± 5.9	42.7 ± 4.3	56.7 ± 4.6	4.8 ± 1.7
4	178.4 ± 26.3	145.8 ± 13.8	76.3 ± 7.8	8.4 ± 1.4
8	350.7 ± 32.2	320.4 ± 29.4	98.6 ± 14.8	7.6 ± 0.7

Evaluation of apoptosis triggered by different nanoparticle systems

The pro-apoptotic effects exerted by the various nanoparticle preparations are captured in **Figure 6**. Representative fluorescence micrographs revealing both the cytoplasmic compartment and the nuclear morphology of treated cells are collected in **Figure 6a**. Cultures of drug-resistant MCF-7/adr cells that had been incubated with either Ce6 nanoparticles or the dual sensitization anti-resistant nanoparticles displayed unmistakable signs of cellular distress: the cytoplasm appeared notably shrunken (red fluorescence signal), and the nuclei had adopted irregular, distorted outlines (blue fluorescence signal). Moreover, cell counts in these two treatment arms were visibly lower than in the other groups, a finding that aligned with previously obtained

cytotoxicity measurements. In agreement with expectations based on their resistant phenotype, MCF-7/adr cells mounted a substantial tolerance response when challenged with free paclitaxel or the paclitaxel-only nanoparticle formulation.

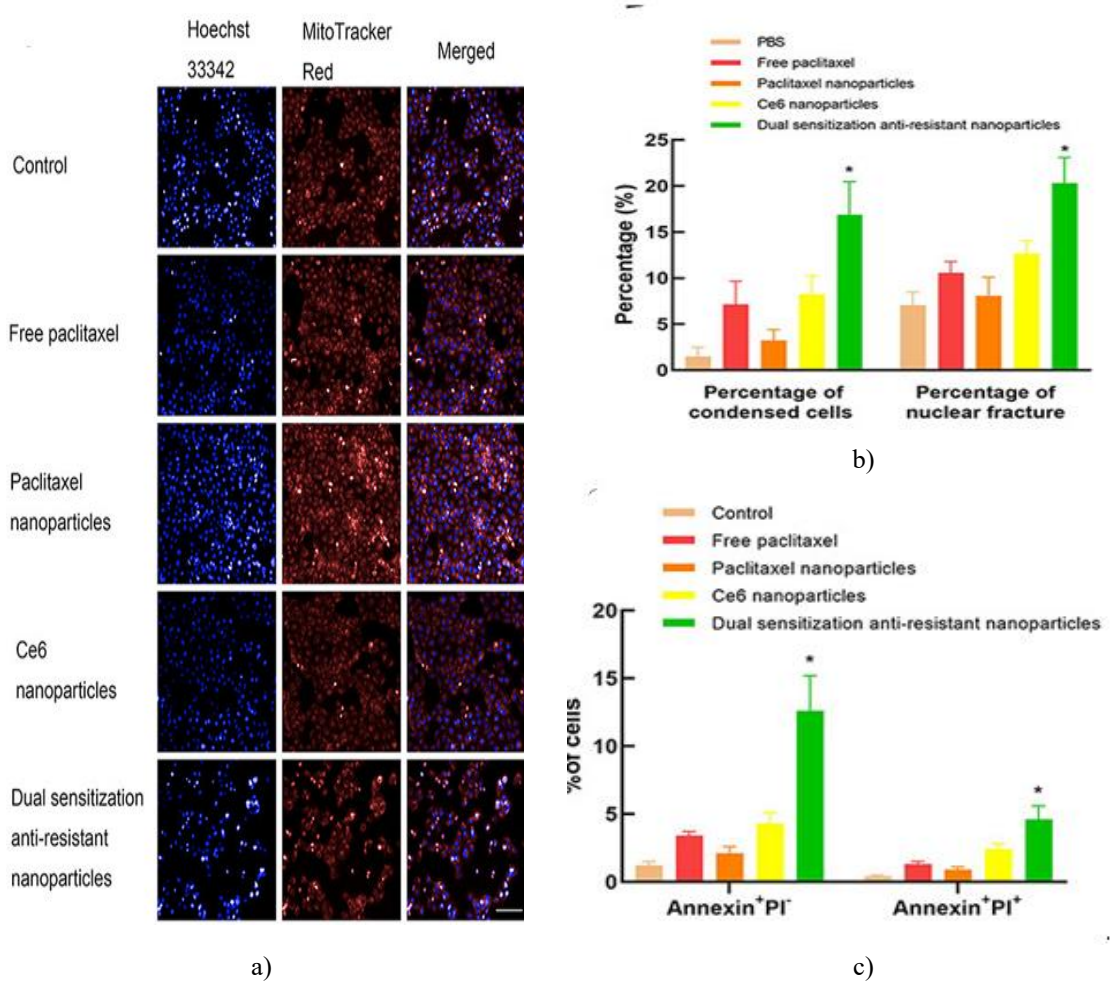

Figure 6. Apoptosis induction by various nanoparticles. Notes: Fluorescence images of the cells and their nuclei (a) were captured by a fluorescence microscope incorporated into the high-content screening system. The drug-resistant MCF-7/adr cells were stained with MitoTracker Red and Hoechst 33342 after being treated with varying nanoparticles. The percentages of condensed cells and nuclear fractures (b) were determined using the Columbus system. Apoptosis of MCF-7/adr cells after treatment was analyzed by flow cytometry following Annexin V/PI staining (c). Scale bar = 100 μm, $P < 0.05$ vs other formulations.

A systematic enumeration of the morphological hallmarks of apoptosis is provided in **Figure 6b.** Arranging the treatment groups by the proportion of cells that had undergone cytoplasmic condensation produced the following hierarchy: dual-sensitization anti-resistant nanoparticles ranked first, followed by Ce6 nanoparticles and free paclitaxel at roughly comparable levels, then paclitaxel nanoparticles, and finally the PBS vehicle control. The same sequence held when nuclear fragmentation was used as the endpoint: dual-sensitization anti-resistant nanoparticles at the top, then Ce6 nanoparticles approximating free paclitaxel, followed by paclitaxel nanoparticles, with PBS registering last. These results made abundantly clear that dual sensitization of anti-resistant nanoparticles drove the most sweeping apoptotic morphological remodeling.

Data from the flow cytometric assessment employing Annexin V and PI as dual markers of apoptosis in MCF-7/adr cells are represented in **Figure 6c.** This staining strategy exploits the fact that cells at an early apoptotic stage externalize phosphatidylserine and bind Annexin V alone. In contrast, cells further along the death pathway lose membrane integrity and become permeable to both fluorophores. When the early apoptotic fraction was ranked across groups, the order was as follows: dual-sensitization anti-resistant nanoparticles > Ce6 nanoparticles ≈ free paclitaxel > paclitaxel nanoparticles > PBS. With respect to the proportion of cells classified as late

apoptotic, the descending sequence shifted slightly to: dual sensitization anti-resistant nanoparticles > Ce6 nanoparticles > free paclitaxel > paclitaxel nanoparticles > PBS. The totality of the flow cytometric evidence reinforced the conclusion that the dual-sensitization anti-resistant nanoparticles outperformed all other formulations tested in driving MCF-7/adr cells toward an apoptotic fate.

Measurement of apoptosis-regulatory protein alterations

Figure 7 collates the quantitative shifts in a panel of proteins involved in apoptosis control in MCF-7/adr cells subjected to the five distinct treatment regimens. Expression and activation levels were normalized to those measured in the normal saline group. For the effector caspase, caspase 3, the relative activity values were as follows: 1.00 ± 0.03 for normal saline, 1.03 ± 0.02 for free paclitaxel, 0.98 ± 0.05 for paclitaxel nanoparticles, 1.18 ± 0.04 for Ce6 nanoparticles, and 1.34 ± 0.04 for the dual-sensitization anti-resistant nanoparticles. The initiator caspase-8 activity ratios were 1.00 ± 0.04 (normal saline), 1.04 ± 0.01 (free paclitaxel), 0.99 ± 0.06 (paclitaxel nanoparticles), 1.12 ± 0.03 (Ce6 nanoparticles), and 1.27 ± 0.03 (dual-sensitization anti-resistant nanoparticles). Caspase 9, the mitochondrial pathway initiator, displayed a corresponding pattern: 1.00 ± 0.06, 1.06 ± 0.02, 1.04 ± 0.04, 1.10 ± 0.02, and 1.23 ± 0.06, respectively. Turning to Bcl-2 family members, the pro-apoptotic effector Bax yielded ratios of 1.00 ± 0.02 (normal saline), 1.07 ± 0.02 (free paclitaxel), 1.06 ± 0.03 (paclitaxel nanoparticles), 1.16 ± 0.02 (Ce6 nanoparticles), and 1.20 ± 0.06 (dual sensitization anti-resistant nanoparticles). The anti-apoptotic guardian Mcl-1, by contrast, showed a divergent trend, with measured ratios of 1.00 ± 0.04 (normal saline), 1.05 ± 0.03 (free paclitaxel), 1.02 ± 0.04 (paclitaxel nanoparticles), 0.88 ± 0.04 (Ce6 nanoparticles), and 0.90 ± 0.04 (dual sensitization anti-resistant nanoparticles)—indicating a downward shift in the two photosensitizer-containing arms. Finally, cytochrome c, a protein released from mitochondria upon apoptotic triggering, exhibited the steepest differential, with activity ratios of 1.00 ± 0.04 (normal saline), 1.06 ± 0.02 (free paclitaxel), 1.05 ± 0.03 (paclitaxel nanoparticles), 1.20 ± 0.04 (Ce6 nanoparticles), and 1.42 ± 0.03 (dual sensitization anti-resistant nanoparticles).

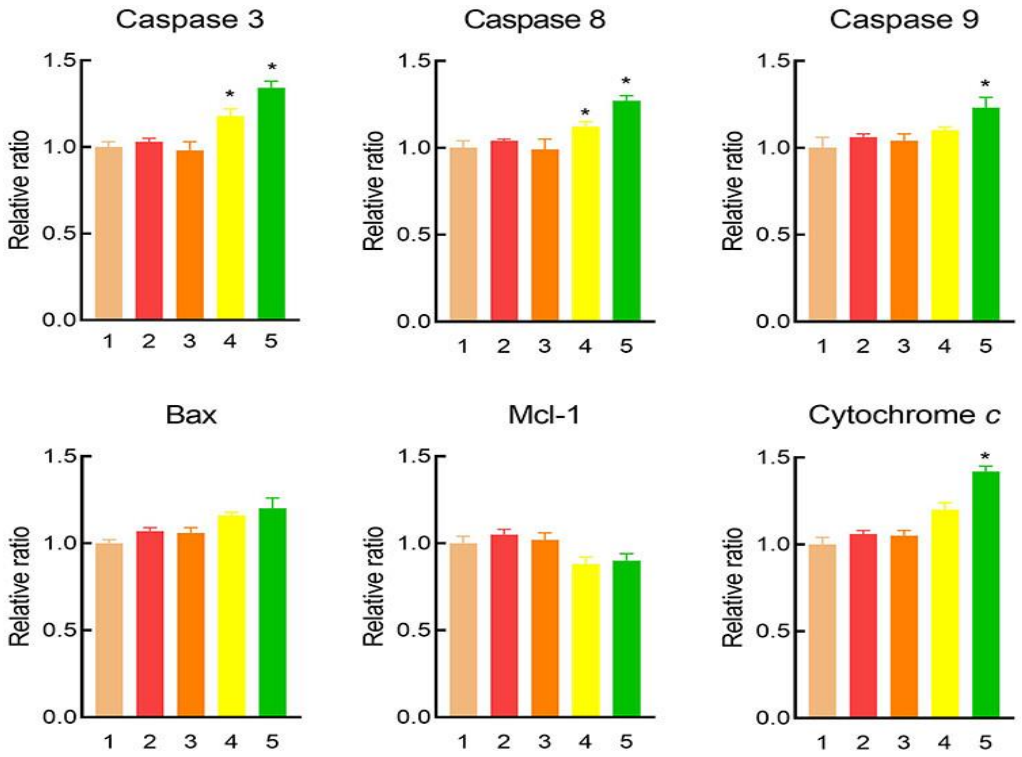

Figure 7. Changes in apoptosis-related proteins in drug-resistant MCF-7/adr cells after treatment with various formulations. Notes: The MCF-7/adr cells were treated with 1) normal saline, 2) free paclitaxel, 3) paclitaxel nanoparticles, 4) Ce6 nanoparticles, and 5) dual sensitization anti-resistant nanoparticles. Data are presented as the mean ± standard deviation (n = 3), $P < 0.05$ vs other formulations.

Therapeutic performance in living animals

The antitumor responses and body weight fluctuations documented in tumor-bearing mice following systemic administration of the different formulations are depicted in **Figure 8.** When assessed at day 24, the hierarchy of relative tumor burden, from least effective to most effective, was as follows: normal saline > free paclitaxel > Ce6 nanoparticles > paclitaxel nanoparticles > dual-sensitization anti-resistant nanoparticles **(Figure 8a).**

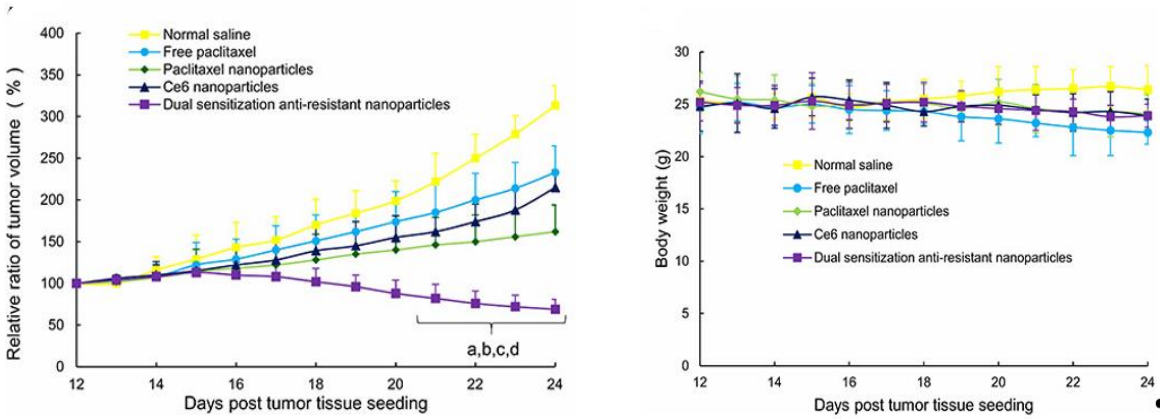

a) b)

Figure 8. Anticancer efficacy (a) and body weight (b) of the tumor-bearing mice after intravenous administration of varying formulations. Notes: Red arrows indicate the drug dosing time points. Data are presented as the mean ± standard deviation (n = 6). a, $P < 0.05$, versus normal saline; b, $P < 0.05$, versus free paclitaxel; c, $P < 0.05$, versus paclitaxel nanoparticles; d, $P < 0.05$, versus dual sensitization anti-resistance nanoparticles.

Body weight measurements across all experimental animals stayed predominantly within the 20–30 g bracket throughout the observation window **(Figure 8b).** A notable exception was the cohort that received free paclitaxel. These mice exhibited a progressive, sustained decline in body mass. This phenomenon can reasonably be ascribed to the organic cosolvent system employed to render the highly lipophilic paclitaxel injectable. In marked contrast, all nanoparticle-based formulations left body weight trajectories essentially unchanged relative to baseline, an outcome that speaks to their favorable tolerability and systemic safety profiles in vivo.

Chemotherapeutic intervention has occupied a central, non-negotiable role in the multipronged clinical approach to managing a wide spectrum of neoplastic diseases for many decades [23-26]. Even as the therapeutic armamentarium has expanded dramatically with the advent of agents targeting previously undruggable molecular vulnerabilities, the overall effectiveness delivered by conventional chemotherapy has remained stubbornly constrained. Outcomes frequently erode over extended treatment cycles, and the tangible clinical benefits realized by patients often prove inadequate. At the root of these disappointments lies the formidable obstacle of multidrug resistance, a phenomenon that manifests in both pre-existing (intrinsic) and treatment-emergent (acquired) guises [27, 28]. The work reported here presents an innovative nanoparticulate platform that holds promise as an alternative means of overcoming drug resistance by leveraging accumulation within neoplastic deposits, boosting cellular entry of the therapeutic cargo, rebalancing the apoptotic machinery, and committing resistant cells to programmed death pathways.

The acquired arm of drug resistance—also referred to as exogenous resistance—arises through iterative cycles of drug challenge. At the molecular level, this process is driven by the escalated expression of ATP-dependent efflux transporters belonging to the ABC superfamily, which line the plasma membrane and actively extrude chemotherapeutic molecules from the intracellular compartment, thereby culminating in the resistant phenotype [29, 30]. In the strategy devised here, paclitaxel was selected as the antineoplastic warhead, and Ce6-TPGS1000 was incorporated as the light-activatable photosensitizer; both were co-formulated into dual-sensitization anti-resistance nanocarriers. The photosensitizer Ce6, in its native, unconjugated state, exhibits poor miscibility with aqueous environments and also serves as a substrate for ABC transporter-mediated outward translocation. Chemically linking Ce6 to the TPGS1000 moiety achieved a twofold objective: it imparted greater hydrophilicity and elevated aqueous solubility. A further benefit emerges once the conjugate undergoes enzymatic processing within the cytoplasm—the TPGS1000 fragment released can thereafter function as a pharmacological inhibitor of multidrug resistance, curtailing the cellular efflux of both Ce6 and the co-administered paclitaxel.

The nanoparticle system constructed in this study had a hydrodynamic diameter centered around 100 nm, a size well matched to the requirements for selective extravasation and retention within the tumor interstitium via the enhanced permeability and retention (EPR) phenomenon [31, 32]. Colloidal drug carriers engineered with surface-displayed targeting ligands are prone to rapid opsonization and clearance by the mononuclear phagocyte system, a process that truncates their circulatory half-life and ultimately blunts therapeutic efficacy [33]. Positively charged nano-delivery platforms, while capable of adhering to tumor-associated vasculature, carry liabilities of pronounced systemic toxicity and preferential hepatic sequestration, factors that together hasten their elimination from the body [34]. The three amphiphilic building blocks—Ce6-TPGS1000, HA-α-TOS, and paclitaxel—could be integrated into a unified nanoparticle architecture through the concerted action of hydrophobic forces, a conclusion supported indirectly by the cooperative anticancer effects observed between photodynamic therapy and chemotherapy **(Figure 3).** A long-standing tenet in colloid science holds that robust nanoparticle stability demands a large absolute zeta potential (exceeding +30 mV or falling below −30 mV); however, this rule rests almost exclusively on considerations of electrostatic double-layer repulsion and fails to account for other stabilizing influences such as van der Waals forces [35]. Particles decorated with polyethylene glycol chains routinely display very modest net surface charge while nonetheless exhibiting excellent resistance to aggregation [36]. The nanocarriers described in this report closely resemble such PEGylated constructs, and their resistance to destabilization was further demonstrated in normal saline and in serum-supplemented medium **(Figure 2e).**

The in vitro cytotoxicity profiling revealed a stark difference in drug responsiveness: the parental MCF-7 line proved substantially more sensitive to the anticancer payload than the MCF-7/adr subline **(Figure 3).** The latter was originally derived through sustained selection pressure with Adriamycin, resulting in the establishment of a stable drug-resistant derivative. Importantly, this resistant cell population remained susceptible to photodynamic challenge. Irradiation with 660 nm light triggered the photodynamic potential of Ce6, and a 10-minute illumination window was sufficient to induce extensive cell death. Given that photodynamic efficacy scales with incident light dose, therapeutic outcomes can be further enhanced by increasing irradiation parameters. The cooperative interaction that emerges when photodynamic damage is superimposed upon chemotherapeutic insult provides yet another avenue for potentiating tumor cell destruction.

The live/dead visualization studies also confirmed that the synergistic cytotoxic action could be governed with exquisite spatial precision. Cell death was sharply restricted to microscopic fields within the illuminated zone; adjacent areas not illuminated by the laser beam exhibited essentially no toxicity. This characteristic provides a direct means to curtail collateral damage to healthy tissues substantially, and thus systemic adverse effects.

Since paclitaxel itself emits no fluorescence under illumination, a hydrophobic fluorophore, coumarin, was substituted as a trackable marker. Coumarin likewise falls within the substrate spectrum of ABC transporter proteins, and the active extrusion of this compound can account for its restricted intracellular accumulation. The progressively smaller gains in fluorescence intensity observed as the incubation was extended from 1 to 8 hours suggested pronounced efflux activity. Relative to free coumarin, the nanoparticulate formulations demonstrated markedly enhanced cellular entry. Endocytic uptake most likely underlies this improvement [37], a notion buttressed by the appearance of discrete punctate fluorescent signals distributed throughout the cytoplasm **(Figure 5a).** Efflux pumps of the ABC superfamily, despite being overexpressed, are capable of handling only low-molecular-weight substrates—among them paclitaxel, adriamycin, and coumarin—and lack the capacity to expel intact nanoparticles that have already gained intracellular access. Consequently, a superior degree of drug internalization was realized. The persistence of bright vesicular spots within the cytoplasmic compartment also implied that the nanoparticles remained structurally coherent following cellular entry.

Programmed cell death, or apoptosis, is the process by which cells undergo ordered self-destruction in response to extrinsic cues, with distinct morphological and biochemical hallmarks characterizing its successive phases. At the earliest stage, phosphatidylserine (PS) residues, which are normally confined to the inner leaflet of the plasma membrane, are externalized to the outer surface, an event detectable by annexin V binding [38]. As apoptosis advances to its later stages, membrane barrier function deteriorates, rendering the nuclei accessible to otherwise membrane-impermeant dyes such as propidium iodide (PI). Cellular contraction and nuclear fragmentation are further characteristic of the late apoptotic phase [39]. Data from the apoptosis detection experiments demonstrated that the dual-sensitization anti-resistant nanoparticles were remarkably effective at driving cells into apoptosis, a potency attributable to the cooperative interplay between photodynamic damage and chemotherapeutic insult **(Figure 6).**

The signaling cascades governing apoptosis can be broadly divided into the extrinsic and intrinsic (mitochondria-centered) branches, each involving distinct protein mediators and enzymatic effectors. Within the extrinsic arm, caspase 8 functions as the apical initiator, whereas caspase 9 fills the corresponding role in the intrinsic route. Once activated, either initiator converges on the downstream executioner caspase 3, which, in turn, sets the irreversible apoptotic cascade in motion [40]. The intrinsic pathway also features opposing activities: Bax, which promotes cell death, and Mcl-1, which restrains it [41]. Release of cytochrome c from the mitochondrial intermembrane space constitutes a sentinel event marking activation of the intrinsic pathway [42]. The pattern of upregulation and downregulation observed across this panel of apoptosis-associated proteins indicated that the dual-sensitization anti-resistant nanoparticles exert their lethal effects by engaging multiple distinct signaling pathways simultaneously **(Figure 7).** For Bax and Mcl-1 activity ratios, statistically significant differences ($P < 0.05$) were observed between the dual-sensitization anti-resistant nanoparticle group and the Ce6 nanoparticle group, compared with the remaining treatment arms. A statistical distinction, however, could not be established between the dual-sensitization anti-resistant nanoparticles and the Ce6 nanoparticles themselves, suggesting a predominant role for photodynamic therapy in mediating these molecular changes.

The therapeutic evaluation conducted in tumor-bearing murine models demonstrated the cooperative antitumor activity of the dual-sensitization anti-resistant nanoparticles in the context of drug-resistant breast cancer **(Figure 8).** The heightened efficacy observed against exogenously acquired resistance may be understood through a multi-step explanatory framework: first, the nanoparticles preserve their colloidal integrity throughout systemic circulation; second, their hydrodynamic dimensions, centered around 100 nm, are conducive to preferential deposition within tumor tissue via the EPR phenomenon; third, cellular internalization is substantially boosted through endocytic mechanisms; fourth, the joint action of photodynamic therapy and chemotherapy can be unleashed upon localized laser application; and finally, the nanoparticles bring about the elimination of the drug-resistant MCF-7/adr cells by steering them into apoptotic cell death.

Conclusion

In the work reported herein, amphiphilic building blocks were synthesized and assembled into dual-sensitization anti-resistant nanoparticles intended to address the challenge of drug-resistant breast cancer. The resulting nanoparticles had a hydrodynamic diameter of roughly 100 nm, displayed favorable colloidal stability, and exhibited only negligible premature drug leakage. They were capable of dramatically augmenting the uptake of both paclitaxel and Ce6 by drug-resistant breast cancer cells and of destroying these cells through the cooperative action of photodynamic therapy operating in tandem with chemotherapy. The activation of multiple signaling pathways triggered apoptosis. Potent antitumor efficacy was demonstrated in tumor-bearing mice, and the nanoparticles exhibited an acceptable biocompatibility and safety profile. Because the robust anticancer effect could be spatially controlled by selective laser irradiation, off-target toxicities were kept to a minimum. Taken together, the present study offers a promising therapeutic strategy that may help to overcome multidrug resistance in the clinical management of breast cancer.

Acknowledgments: This work was financially supported by China Postdoctoral Science Foundation (2019M653973); National Youth Science Fund Project (81703453), Beijing Municipal Education Commission Science and Technology Plan General Project (KM201810017002), and Beijing Excellent Talent Cultivation Independent Project (201600002012G058).

Conflict of Interest: None

Financial Support: None

Ethics Statement: None

References

1. Fahad Ullah MF. Breast cancer: Current perspectives on the disease status. Adv Exp Med Biol. 2019;1152:51-64.
2. Kim MY. Breast cancer metastasis. Adv Exp Med Biol. 2021;1187:183-204.

3. Nedeljković M, Damjanović A. Mechanisms of chemotherapy resistance in triple-negative breast cancer: How we can rise to the challenge. Cells. 2019;8(9):957.
4. Gote V, Nookala AR, Bolla PK, Pal D. Drug resistance in metastatic breast cancer: Tumor-targeted nanomedicine to the rescue. Int J Mol Sci. 2021;22(9):4673.
5. Wu Q, Yang Z, Nie Y, Shi Y, Fan D. Multi-drug resistance in cancer chemotherapeutics: Mechanisms and lab approaches. Cancer Lett. 2014;347(2):159-66.
6. Kartal-Yandim M, Adan-Gokbulut A, Baran Y. Molecular mechanisms of drug resistance and its reversal in cancer. Crit Rev Biotechnol. 2016;36(4):716-26.
7. Zheng HC. The molecular mechanisms of chemoresistance in cancers. Oncotarget. 2017;8(35):59950-64.
8. Champeau M, Vignoud S, Mortier L, Mordon S. Photodynamic therapy for skin cancer: How to enhance drug penetration? J Photochem Photobiol B. 2019;197:111544.
9. Dolmans DE, Fukumura D, Jain RK. Photodynamic therapy for cancer. Nat Rev Cancer. 2003;3(5):380-7.
10. Kumari P, Paul M, Bhatt H, Maiti M, Shukla S, Mishra AK, et al. Chlorin e6 conjugated methoxy-poly(ethylene glycol)-poly(D,L-lactide) glutathione sensitive micelles for photodynamic therapy. Pharm Res. 2020;37(2):18.
11. Jalde SS, Chauhan AK, Lee JH, Chaturvedi PK, Park JS, Kim YW. Synthesis of novel chlorin e6-curcumin conjugates as photosensitizers for photodynamic therapy against pancreatic carcinoma. Eur J Med Chem. 2018;147:66-76.
12. Shanmugam V, Selvakumar S, Yeh CS. Near-infrared light-responsive nanomaterials in cancer therapeutics. Chem Soc Rev. 2014;43(17):6254-87.
13. Choudhury H, Gorain B, Pandey M, Chatterjee LA, Sengupta P, Das A, et al. Recent advances in TPGS-based nanoparticles of docetaxel for improved chemotherapy. Int J Pharm. 2017;529(1-2):506-22.
14. Yan H, Du X, Wang R, Zhai G. Progress in the study of D-α-tocopherol polyethylene glycol 1000 succinate (TPGS) reversing multidrug resistance. Colloids Surf B Biointerfaces. 2021;205:111914.
15. Bayer IS. Hyaluronic acid and controlled release: A review. Molecules. 2020;25(11):2649.
16. Abatangelo G, Vindigni V, Avruscio G, Pandis L, Brun P. Hyaluronic acid: Redefining its role. Cells. 2020;9(7):1743.
17. Rezaei S, Kashanian S, Bahrami Y, Cruz LJ, Motiei M. Redox-sensitive and hyaluronic acid-functionalized nanoparticles for improving breast cancer treatment by cytoplasmic 17α-methyltestosterone delivery. Molecules. 2020;25(5):1135.
18. Bernabeu E, Cagel M, Lagomarsino E, Moretton M, Chiappetta DA. Paclitaxel: What has been done and the challenges remain ahead. Int J Pharm. 2017;526(1-2):474-95.
19. Sofias AM, Dunne M, Storm G, Allen C. The battle of "nano" paclitaxel. Adv Drug Deliv Rev. 2017;122:20-30.
20. Haggag Y, Abu Ras B, El-Tanani Y, Tambuwala MM, McCarron P, Isreb M, et al. Co-delivery of a RanGTP inhibitory peptide and doxorubicin using dual-loaded liposomal carriers to combat chemotherapeutic resistance in breast cancer cells. Expert Opin Drug Deliv. 2020;17(11):1655-69.
21. Haggag YA, Yasser M, Tambuwala MM, El Tokhy SS, Isreb M, Donia AA. Repurposing of guanabenz acetate by encapsulation into long-circulating nanopolymersomes for treatment of triple-negative breast cancer. Int J Pharm. 2021;600:120532.
22. Haggag YA, Abosalha AK, Tambuwala MM, Osman EY, El-Gizawy SA, Essa EA, et al. Polymeric nanoencapsulation of zaleplon into PLGA nanoparticles for enhanced pharmacokinetics and pharmacological activity. Biopharm Drug Dispos. 2021;42(1):12-23.
23. Hurwitz M. Chemotherapy in prostate cancer. Curr Oncol Rep. 2015;17(10):44.
24. Kim JH. Chemotherapy for colorectal cancer in the elderly. World J Gastroenterol. 2015;21(17):5158-66.
25. Marsh S, Liu G. Pharmacokinetics and pharmacogenomics in breast cancer chemotherapy. Adv Drug Deliv Rev. 2009;61(5):381-7.
26. Roett MA, Evans P. Ovarian cancer: An overview. Am Fam Physician. 2009;80(6):609-16.
27. Bukowski K, Kciuk M, Kontek R. Mechanisms of multidrug resistance in cancer chemotherapy. Int J Mol Sci. 2020;21(9):3233.
28. Szakács G, Paterson JK, Ludwig JA, Booth-Genthe C, Gottesman MM. Targeting multidrug resistance in cancer. Nat Rev Drug Discov. 2006;5(3):219-34.
29. Liu X. ABC family transporters. Adv Exp Med Biol. 2019;1141:13-100.

30. Choi YH, Yu AM. ABC transporters in multidrug resistance and pharmacokinetics, and strategies for drug development. Curr Pharm Des. 2014;20(5):793-807.
31. Maeda H, Wu J, Sawa T, Matsumura Y, Hori K. Tumor vascular permeability and the EPR effect in macromolecular therapeutics: A review. J Control Release. 2000;65(1-2):271-84.
32. Subhan MA, Yalamarty SSK, Filipczak N, Parveen F, Torchilin VP. Recent advances in tumor targeting via EPR effect for cancer treatment. J Pers Med. 2021;11(6):535.
33. Bao J, Zhang Q, Duan T, Hu R, Tang J. The fate of nanoparticles in vivo and the strategy of designing stealth nanoparticle for drug delivery. Curr Drug Targets. 2021;22(8):922-46.
34. Kalyanaraman B, Cheng G, Hardy M, Ouari O, Lopez M, Joseph J, et al. A review of the basics of mitochondrial bioenergetics, metabolism, and related signaling pathways in cancer cells: Therapeutic targeting of tumor mitochondria with lipophilic cationic compounds. Redox Biol. 2018;14:316-27.
35. Bhattacharjee S. DLS and zeta potential—What they are and what they are not? J Control Release. 2016;235:337-51.
36. Gabizon A, Martin F. Polyethylene glycol-coated (pegylated) liposomal doxorubicin. Rationale for use in solid tumours. Drugs. 1997;54 Suppl 4:15-21.
37. Oh N, Park JH. Endocytosis and exocytosis of nanoparticles in mammalian cells. Int J Nanomedicine. 2014;9 Suppl 1:51-63.
38. Crowley LC, Marfell BJ, Scott AP, Waterhouse NJ. Quantitation of apoptosis and necrosis by annexin V binding, propidium iodide uptake, and flow cytometry. Cold Spring Harb Protoc. 2016;2016(11):pdb.prot087288.
39. Tengku Din TA, Seeni A, Khairi WN, Shamsuddin S, Jaafar H. Effects of rapamycin on cell apoptosis in MCF-7 human breast cancer cells. Asian Pac J Cancer Prev. 2014;15(24):10659-63.
40. Shi Y. Mechanisms of caspase activation and inhibition during apoptosis. Mol Cell. 2002;9(3):459-70.
41. Bruckheimer EM, Cho SH, Sarkiss M, Herrmann J, McDonnell TJ. The Bcl-2 gene family and apoptosis. Adv Biochem Eng Biotechnol. 1998;62:75-105.
42. Ow YP, Green DR, Hao Z, Mak TW. Cytochrome c: Functions beyond respiration. Nat Rev Mol Cell Biol. 2008;9(7):532-42.